Reaction Chemistry
& Engineering

Proton Exchange Membrane Flow Reactor with Ozone-Treated Gas Diffusion Layers for Production of Pure H_2O_2 in Aqueous and Methanol Solutions

Journal:	*Reaction Chemistry & Engineering*
Manuscript ID	RE-ART-12-2024-000634.R1
Article Type:	Paper
Date Submitted by the Author:	01-Apr-2025
Complete List of Authors:	Okazaki, Takuya; Tokyo Metropolitan University, Department of Applied Chemistry for Environment Tateishi, Chihiro; The University of Kitakyushu Shibata, Kento; The University of Kitakyushu Enomoto, Kazuma; Tokyo Metropolitan University, Department of Applied Chemistry for Environment Amano, Fumiaki; Tokyo Metropolitan University, Department of Applied Chemistry for Environment

ARTICLE

Proton Exchange Membrane Flow Reactor with Ozone-Treated Gas Diffusion Layers for Production of Pure H_2O_2 in Aqueous and Methanol Solutions

Received 00th January 20xx,
Accepted 00th January 20xx

DOI: 10.1039/x0xx00000x

Takuya Okazaki,[a] Chihiro Tateishi,[b] Kento Shibata,[b] Kazuma Enomoto,[a] and Fumiaki Amano*[a]

Electrocatalytic production of pure H_2O_2 via a two-electron oxygen reduction reaction (2e⁻ ORR) in a proton exchange membrane (PEM) flow reactor is an ideal process for on-site and on-demand H_2O_2 usage. However, the low selectivity is challenging due to the successive reduction of generated H_2O_2 remaining on the electrocatalyst in membrane electrode assembly with gas diffusion layer (GDL). This study investigates selective 2e⁻ ORR in an H_2–O_2 PEM flow reactor (PEMFR) using a cobalt electrocatalyst with various cathode GDLs to optimize the transport of solvent to recover the generated H_2O_2. The effects of wettability and hydrophobicity were tested using pristine, polytetrafluoroethylene (PTFE) treated, and ozone-treated carbon GDLs under simultaneous water and O_2 gas flow. The ozone-treated GDL, with slight hydrophilicity, continuously produced 46 mM H_2O_2 (1560 ppm) with a Faradaic efficiency (FE) of ~75% at a current density of 20–30 mA cm^{-2}. In contrast, pristine and PTFE-treated GDLs resulted in low H_2O_2 FE below 15%. The ozone-treated GDL on the flow channel side was critical for transporting liquid water to recover the generated H_2O_2. The production of H_2O_2 in methanol instead of water also achieved ~80% FE, without applying energy bias.

Introduction

Hydrogen peroxide (H_2O_2) is an eco-friendly oxidizing agent used in disinfection, pulp and paper bleaching, water treatment, and chemical synthesis.[1–4] The anthraquinone process, the main industrial method for H_2O_2 production, is a centralized batch process with complex infrastructure and high costs.[1,5] While high concentrations are needed for cost-effective transport, this poses an explosion risk.[1,6] Since H_2O_2 is typically used in diluted form, a delocalized on-site production is preferable for the demands.

Electrocatalytic H_2O_2 production through a two-electron oxygen reduction reaction (2e⁻ ORR) has been proposed for on-site and small-scale applications.[7–9] The ORR proceeds via two pathways (2e⁻ and 4e⁻) producing H_2O_2 and water, respectively, as follows:[1,10]

$$\mathrm{O_2 + 2H^+ + 2e^- \rightarrow H_2O_2},\ E^0 = 0.70\ \mathrm{V\ vs.\ RHE} \qquad (1)$$

$$\mathrm{O_2 + 4H^+ + 4e^- \rightarrow 2H_2O},\ E^0 = 1.23\ \mathrm{V\ vs.\ RHE} \qquad (2)$$

Various electrocatalysts including metals, metal oxides, carbon materials, and single-atom catalysts (SACs) have been developed for H_2O_2 production.[10] The performance of electrocatalysts is typically investigated by hydrodynamic voltammetry using rotating ring disk electrodes (RRDE), which provides an upper limit on H_2O_2 Faradaic efficiency (FE).[1] The actual H_2O_2 production is usually evaluated in H-type two-compartment cells.[8,11,12]

In proton exchange membrane (PEM) fuel cells, a gas diffusion layer (GDL), typically made of porous carbon fiber paper or carbon cloth, ensures efficient gas distribution across the catalyst surface, enhancing O_2 mass transport.[13,14] Even in the 2e⁻ ORR, the hydrophobicity of GDL is critical for overcoming diffusion limitations caused by low O_2 solubility in water.[12,15,16] GDLs also conduct electrons with low resistance and reduce interfacial contact resistance.[14] Gas diffusion electrode (GDE)-based three-compartment cells, typically comprising an O_2 flow cathode chamber, a liquid catholyte chamber, a polymer electrolyte membrane, and an anolyte chamber, have also been developed.[17–19] The catholyte chamber provides ion conductivity and collects H_2O_2 produced on the catalyst surface.

Electrocatalytic 2e⁻ ORR without using electrolyte solutions has also been studied for H_2O_2 production, eliminating the need for neutralization and purification.[10] Pure H_2O_2 production in PEM cells, rather than liquid electrolytes, is ideal for on-site and on-demand applications, suitable for water treatment and organic synthesis in solvents like methanol. Furthermore, compared to batch-type reactors, flow-type PEM reactors allow for continuous H_2O_2 production. However, the high FE for 2e⁻ ORR observed in the RRDE experiment often decreases in the PEM cell due to the transport limitations of the produced H_2O_2.[1]

---

[a] Department of Applied Chemistry for Environment, Tokyo Metropolitan University, Tokyo 192-0397, Japan.

[b] Department of Chemical and Environmental Engineering, The University of Kitakyushu, Fukuoka 808-0135, Japan.

Supplementary Information available: Calibration curve for H_2O_2 analysis, SEM and EDS images, Cyclic voltammograms, Effect of pretreatment (PDF). See DOI: 10.1039/x0xx00000x

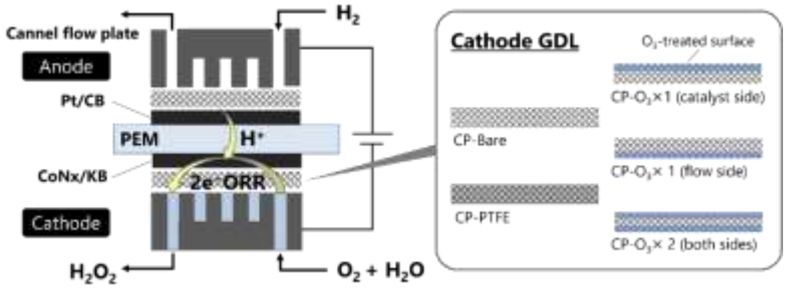

Figure 1. H_2–O_2 fuel cell-type PEMFR for pure H_2O_2 production under simultaneous flow of O_2 gas (50 mL min^{-1}) and water (0.50 mL min^{-1}).

Increased local concentration of H_2O_2 near the membrane can accelerate its decomposition,[1] as represented by Eq. 3:[20]

$$\mathrm{H_2O_2 + 2H^+ + 2e^- \rightarrow 2H_2O},\ \ E^0 = 1.76\ \mathrm{V\ vs.\ RHE} \qquad (3)$$

Yamanaka et al. pioneered the use of PEM cells for neutral H_2O_2 production, achieving concentrations up to 5.5 M (18.7 wt%) in batch-type cells.[21] They attributed the decrease in FE from 100% in RRDE to 55% in the PEM cell to H_2O_2 reduction during water transport through the membrane. Wang et al. improved H_2O_2 production efficiency using a three-compartment cell with a porous solid electrolyte (ion exchange resin particles) instead of liquid electrolytes, achieving pure H_2O_2 at 3.4 mmol cm^{-2} h^{-1} with 90% FE.[8] However, the low ion conductivity of the resin between the electrode gap resulted in increased cell voltage. Wilkinson et al. studied the effects of Teflon content, water flow rate, and cobalt-carbon catalyst loading on the H_2O_2 production in a zero-gap PEM cell at 60°C, observing a decrease in H_2O_2 FE from 50% to 30% as current density increased.[22,23] Geyer et al. explored platinum diphosphide nanocrystals as an electrocatalyst in a zero-gap PEM cell, finding 79% FE at 40°C, which decreased to 54% at room temperature, both lower than the 98.5% FE from RRDE experiments.[24] The zero-gap proton exchange membrane flow reactor (PEMFR) provides low cell resistance required for practical electrochemical applications, but its design strategy remains undeveloped for high FE for 2e⁻ ORR.

In this study, we investigated pure H_2O_2 production in a zero-gap PEMFR using a variety of GDLs to optimize solvent transport for efficient H_2O_2 recovery (Fig. 1). In polymer electrolyte fuel cells (PEFCs) and water electrolyzers, controlling the hydrophobicity and hydrophilicity of the GDL or porous transport layer (PTL) is crucial for maintaining triple-phase boundaries (TPBs) between reactant gas, catalyst, and proton-conducting ionomer.[25,26] In PEFCs, managing water at the cathode, produced by ORR or transported through the PEM with protons, is essential to prevent GDL flooding and PEM drying.[27,28] Thus, we focused on the effect of GDL wettability on continuous H_2O_2 production in the H_2–O_2 fuel cell-type PEMFR. We tested three types of GDLs (pristine carbon paper, polytetrafluoroethylene (PTFE) loaded, and ozone treated) with different wettability. The ozone-treated carbon surface contains hydrophilic functional groups.[29] We also proposed electrocatalytic H_2O_2 production in methanol as an alternative solvent in the zero-gap PEMFR.

Experimental

Preparation of the electrocatalyst

A cobalt SAC for 2e⁻ ORR was prepared by modifying the method of Yamanaka et al.[20,21] A Ketjen Black (KB; Carbon ECP600JD) powder was impregnated with an ethanol solution of cobalt(II)-tetraphenylporphyrin (Co-TPP), dissolved by ultrasonication. The cobalt loading on KB was 0.05 wt%. The mixture was dried at 80°C to evaporate the solvent and then calcined in a tube furnace at 750°C for 2 h under a N_2 flow of 100 mL min^{-1}. The thermally processed sample is denoted as CoN$_x$/KB. The characterization techniques revealed that the cobalt species is stabilized on KB via 2 or 3 nitrogen atoms without Co-Co agglomeration.[12] The electrochemical performance in electrolytes with pH ranging from acidic to alkaline was also studied using the RRDE and a GDL-based H-type cell.[12]

Preparation of the catalyst films

To prepare a cathode catalyst ink, 31 mg of CoN$_x$/KB and 0.66 mL of 5 wt% Nafion ionomer solution (D-520) were added to a mixture of 1.2 mL of 1-propanol, 7.2 mL of 2-propanol and 0.50 mL of water. This mixture was dispersed using an ultrasonic bath and ultrasonic homogenizer (SLPe, Branson). The ionomer-to-carbon (I/C) weight ratio was 1.0. A catalyst slurry was prepared by evaporating the solvent while mixing it with a planetary centrifugal mixer (AR-100, Thinky). The CoN$_x$/KB film was formed by applying the catalyst ink onto a 0.05 × 65 × 65 mm plasma-treated PTFE sheet (0.13 mm thick) using a bar coater (MC20, Hohsen), with a catalyst loading of 0.2 mg cm^{-2}. The anode catalyst film was prepared similarly, using 61 mg Pt/CB catalyst (Pt 46.6wt%, Tanaka Kikinzoku Kogyo) and Nafion ionomer, maintaining the I/C ratio of 1.0. The Pt/CB loading was 0.2 mg cm^{-2} on the PTFE sheet.

Preparation of the MEA

The CoN$_x$/KB film (20 × 20 mm) supported on a PTFE sheet was centered on a 50 × 50 mm Nafion membrane (N117, DuPont) with a 0.05 mm-thick PTFE (20 × 20 mm). The CoN$_x$/KB and Nafion sheets were hot-pressed at 140°C and 15 kN between PTFE sheets with copper plates for 1 min, with four cycles of 90-degree rotations. The Pt/CB sheet was similarly hot pressed onto the Nafion side opposite the CoN$_x$/KB catalyst side. The PTFE sheets were removed from the catalyst surface of the hot-pressed MEA.

Preparation of the GDLs

Carbon paper GDLs (SGL carbon, 280 μm thick) were obtained from MFC technology. The pristine carbon paper (CP-Bare) is Sigracet 39AA. The PTFE-treated carbon paper (CP-PTFE) is Sigracet 39BA, with 5 wt% PTFE loading. Ozone-treated carbon paper (CP-O_3) was prepared from CP-Bare using an ozone reactor (ASM401N, Asumi Giken) with a 40 W low-pressure mercury lamp. The ozone treatment was performed for 2.0 min on one side of CP-Bare under the 254-nm ultraviolet (UV) irradiation in the air at room temperature. The GDL treated on one side is denoted as CP-O_3×1, while treatment on both sides is denoted as CP-O_3×2 as shown in Fig. 1. In all experiments, CP-PTFE was used as the anode GDL. The MEA and GDLs were assembled in a planar stainless-steel cell with a 4 $\mathrm{cm_{geo}^2}$ electrode area.

Electrochemical H_2O_2 production

H_2–O_2 PEMFR was operated in a two-electrode zero-gap configuration using an electrochemical measurement system (HZ-PRO S4, Hokuto Denko). The humidified O_2 through a bubbler filled with deionized water was supplied to the cathode in the MEA cell at a typical flow rate of 50 mL $\mathrm{min^{-1}}$. Deionized water or methanol was supplied to the cathode at a flow rate of 0.50 mL $\mathrm{min^{-1}}$ by a pump (NP-KX-500, Nihon Seimitsu Kagaku) in the common flow line with O_2 gas through a T-tube. A humidified H_2 was supplied to the Pt/CB anode at 20 mL $\mathrm{min^{-1}}$ for the hydrogen oxidation reaction (HOR). When H_2, the fuel, is oxidized at the anode, the system operates in *fuel cell mode* and does not require power input; instead, power is generated.[23] In contrast to *electrolysis mode*, where power input is needed to oxidize water at the anode. The H_2–O_2 PEMFR operates in a *fuel cell mode*, and the operating voltage (typically ΔE = 0.10 V) was controlled by the electrochemical system. Before the reaction, the cathode was purged with 50 mL $\mathrm{min^{-1}}$ humidified O_2 for 1 h, then pretreated with 5.0 mL $\mathrm{min^{-1}}$ water for 10 min, otherwise noted. The water flow rate was then switched to 0.5 mL $\mathrm{min^{-1}}$, and O_2 gas was simultaneously introduced at a flow rate of 50 mL $\mathrm{min^{-1}}$.

The yield of H_2O_2 in outlet water was determined by $KMnO_4$ titration. The change in oxidation-reduction potential while adding 2.0 mmol $\mathrm{L^{-1}}$ $KMnO_4$ solution was measured using an automatic potentiometric titrator (Eco Titrator, Metrohm). In methanol, the concentration of H_2O_2 was measured by spectrophotometry based on the potassium iodide method since methanol itself is oxidized by $KMnO_4$. To a 2.0 mL sample, 1.0 mL of 0.1 M potassium hydrogen phthalate solution (pH 4.0) and 1.0 mL of 1.0 M potassium iodide solution were added and stirred at room temperature for 1 h. The sample was then diluted 100-fold with methanol, and the absorbance of the solution was measured using a spectrophotometer (Shimadzu, UV-2600). The absorption spectra for the calibration samples and the linear calibration curve with respect to the H_2O_2 concentration in methanol are shown in Fig. S1. The FE of H_2O_2 was obtained using Eq. 4.

$$\mathrm{FE}\ [\%] = \frac{y \times n \times F}{I \times t} \times 100 \qquad (4)$$

where y: yield of H_2O_2, n: number of electrons (*i.e.,* 2 in the 2e^- ORR), F: Faraday constant, I: current at a specific cell voltage, and t: reaction time.

Characterization

The surface of the GDLs and the cross-section of the MEA were observed using a field emission scanning electron microscope (FE-SEM, JSM-7800F and JSM-IT800, JEOL) with an energy-dispersive X-ray spectroscopic (EDS) analyzer. The MEA was sputtered with Au before SEM observation. X-ray photoelectron spectroscopy (XPS) analysis was carried out using an AXIS-HSi (Shimadzu) with Mg-Kα source in voltage of 12 kV. The contact angle of the GDLs was measured using a contact angle meter (LSE-B100W, Nick Co.) with a 3.5 μL droplet, recorded 5 seconds after dispensing.

Results and discussion

Characterization of the GDLs and MEA

Figure 2 shows the contact angles of the GDLs. The contact angles of the CP-Bare, CP-PTFE, and treated side and back side of CP-O_3×1 were 131, 137, 100, and 132 degrees, respectively. These indicate higher hydrophobicity in CP-PTFE compared to CP-Bare due to the PTFE loading. The ozone treatment on CP-O_3×1 for 2.0 min slightly enhanced wettability, while the untreated side maintained the same properties as the CP-Bare. Increasing the ozone treatment time increases wettability.

SEM images revealed no significant differences in the surface morphology of carbon fibers and fillers, indicating that the ozone treatment did not affect the GDL material (Figure S2). The SEM-EDS analysis showed the mass ratio was 100 mass% on the CP-Bare and CP-O_3×1, and the presence of fluorine on CP-PTFE (82 mass% carbon and 18 mass% fluorine). The elemental mapping reveals a uniform distribution of fluorine across both the fibers and fillers in CP-PTFE, indicating uniform coverage of PTFE throughout the structure.

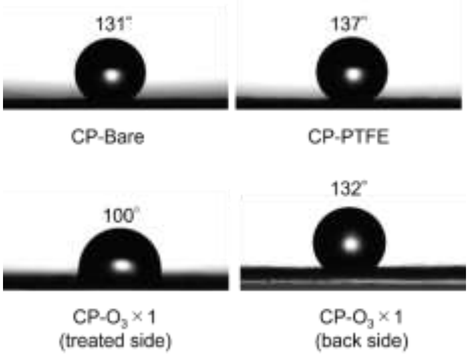

Figure 2. Photographs of contact angle measurement of CP-Bare, CP-PTFE, and CP-O_3×1 (O_3-treated surface and its reverse side). The ozone treatment was performed for CP-Bare for 2.0 min.

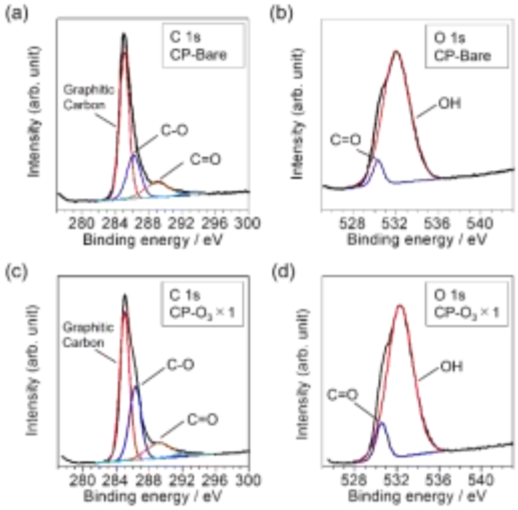

Figure 3. C 1s and O 1s XPS spectra of the CP-Bare (a, b) and CP-O_3×1 (c, d).

Table 1. Relative atomic concentrations (%) of GDL surfaces determined by XPS

	C 1s			O 1s	
GDL	Graphitic	C–O	C=O	O–H	carbonate
CP-Bare	59.4	25.2	15.4	93.3	6.7
CP-O_3×1	53.3	32.5	14.2	90.5	9.5

The CP-Bare and CP-O_3×1 were analyzed by XPS to investigate the effect of the ozone treatment. Figure 3 shows the XPS spectra for the chemical states of C 1s and O 1s of CP-Bare and CP-O_3. The deconvoluted C 1s spectrum exhibits contributions from graphitic carbon (284.8 eV), C–O (285.9 eV), and C=O (288.7 eV) functional groups. The O 1s peaks are attributed to hydroxide (O–H, 531.7 eV) and carbonate (C=O/C–O, 530.0 eV) species. Table 1 shows XPS-derived relative atomic concentration, demonstrating ~7% increase in C–O in the C 1s region for CP-O_3×1. The ozone treatment increased the surface concentration of carboxyl and hydroxyl groups, enhancing hydrophilicity.[29,30]

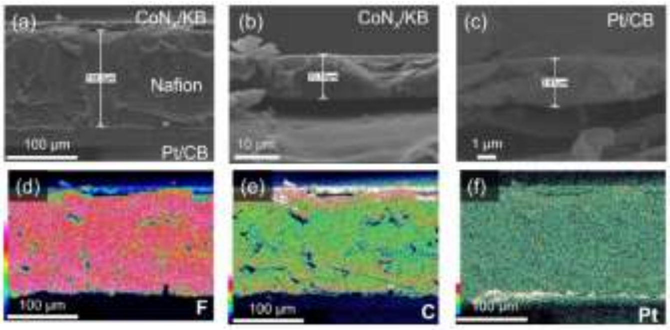

Figure 4. Scanning electron microscope image of a cross-section of the membrane electrode assembly (a) and its CoN$_x$/KB (b) and Pt/CB layers (c). EDS mapping of fluorine (d), carbon (e), and platinum (f).

Figure 4 shows cross-sectional FE-SEM images and EDS elemental mapping of the MEA. Three distinct layers of CoN$_x$/KB, Nafion, and Pt/CB were observed from the top to bottom of the image. The thicknesses of CoN$_x$/KB and Pt/CB layers in the MEA were estimated to be approximately 10 µm and 2.5 µm, respectively. The EDS's elemental mapping of fluorine, carbon, and platinum shows the separation of each layer.

H_2O_2 production in the PEMFR

Supply of oxygen to the PEMFR The O_2 supply to the cathode in the zero-gap PEMFR was investigated using the MEA consisting of CoN$_x$/KB, Nafion membrane, and Pt/CB layers. Figure 5 (a) shows the cyclic voltammograms comparing "simultaneous O_2 gas and water flow" with "O_2-purged water flow" in the PEMFR using CP-PTFE as the GDL. The current density was significantly higher with the simultaneous flow of O_2 gas and water, indicating sufficient O_2 supply to the CoN$_x$/KB layer. In contrast, O_2-purged water flow resulted in lower current density, confirming insufficient dissolved O_2 for the ORR reaction. Given the low solubility of O_2 in water (1.3 mmol L^{-1}),[31] the cyclic voltammogram with O_2-purged water showed negligible ORR and a diffusion-limited current at ~0.1 V, as shown in the expanded inset. In contrast, the simultaneous O_2 gas and water flow achieved a current density of 18 mA cm^{-2} at 0 V, with an exponential curve following the Butler-Volmer relationship. This result suggests that sufficient O_2 supply formed TPBs at the interface between O_2 gas, electrocatalyst, and water. The significant increase in current density with gaseous O_2 supply instead of dissolved O_2 aligns with previous results, where CP-PTFE loaded with CoN$_x$/KB as a GDE immersed in aqueous electrolytes showed current densities of 100 mA cm^{-2} level for H_2O_2 production in an H-type glass cell.[12] When dissolved O_2 was used instead, the current density dropped drastically.

The current-time curve at 0.10 V in fuel cell mode showed that the current density gradually decreased from 10 to 3 mA cm^{-2} for 4 h (Fig. 5 (b)). The FE of H_2O_2 was low, around 10%, when using CP-PTFE as the GDL (Fig. 5(c)). This low FE may be attributed to the fact that the H_2O_2 generated on the electrocatalyst surface was successively reduced as proposed in Eq. 3.[1,8,21] In contrast, the H-type cell with CoNx/KB catalyst on the CP-PTFE GDL achieved an H_2O_2 FE of around 80%,[12] because the electrocatalyst surface was immersed in the stirred electrolyte solution, preventing H_2O_2 from being retained and successively reduced. This finding emphasizes the importance of the removal of the generated H_2O_2 from the electrocatalyst surface by water flow to improve the H_2O_2 FE. In the PEMFR for $2e^-$ ORR, the hydrophobicity of the conventional GDLs (CP-PTFE with and without microporous layer) prevented sufficient water flow to the electrocatalyst surface, resulting in the negligible H_2O_2 FE. The retention of the generated H_2O_2 on the surface causes successive reduction into water.

Wettability and hydrophobicity of the GDL To improve H_2O_2 FE in the PEMFR, the cathode GDLs, including CP-Bare and CP-O_3×1, were evaluated with a simultaneous supply of water (0.50 mL min^{-1}) and gaseous O_2 (50 mL min^{-1}). The GDLs were pretreated with water for 10 min before PEMFR operation to achieve a steady-state condition. The ozone-treated side of the CP-O_3×1 was placed facing the cathode flow channel. The cyclic voltammetry curves after the pretreatment showed almost no change for each GDL (Fig. S3(a)), suggesting that O_2 gas was adequately supplied to the electrocatalyst. Current-time curves

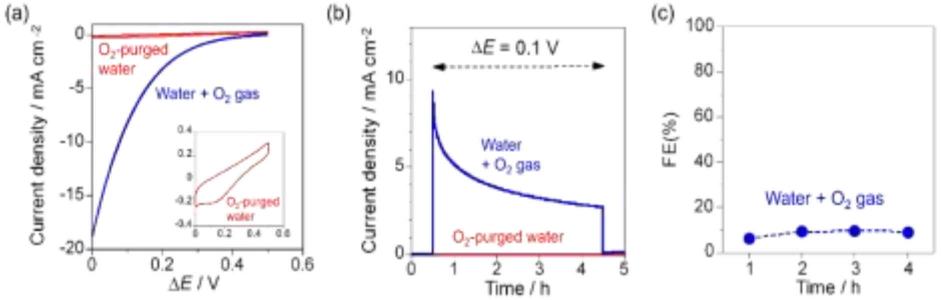

Figure 5. Cyclic voltammograms (a), current-time curves at an operating voltage of 0.10 V (b), and FE of H_2O_2 production (c) in a fuel cell mode with simultaneous flows of O_2 gas and water at 50- and 0.50-mL min^{-1}, respectively, and with a flow of O_2-purged water at 0.50 mL min^{-1} into the cathode of the PEMFR with CP-PTFE.

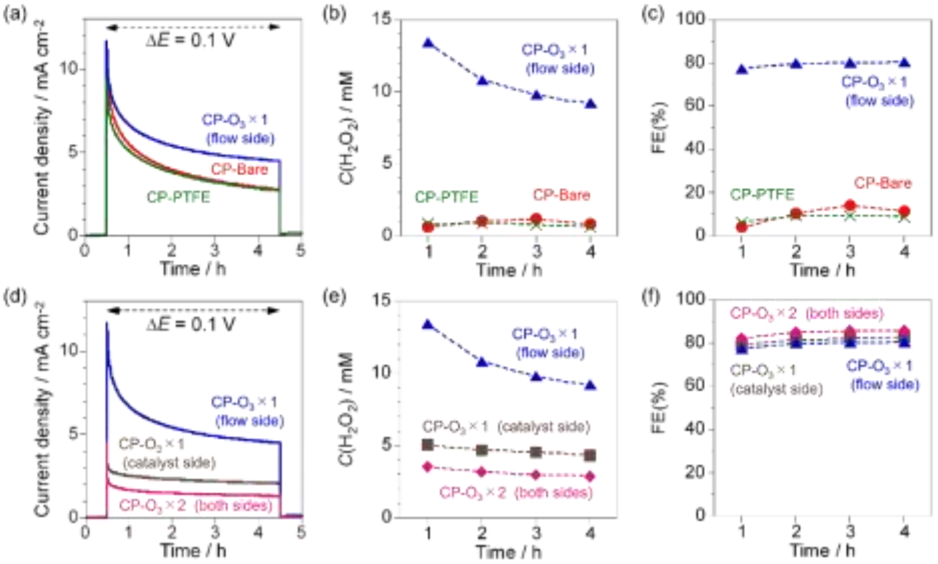

Figure 6. Current-time curves of the PEMFR with CP-Bare, CP-PTFE, CP-O_3 electrode (a) and CP-O_3 GDLs with different orientations of ozone-treated side (b) at an operating voltage of 0.10 V. Concentrations of produced H_2O_2 (b, e) and FE (c, f). O_2 and water simultaneously flowed into the cathode at 50- and 0.50-mL min^{-1}, respectively.

at 0.10 V showed gradual decreases in the current density during ORR (Fig. 6 (a)). The PEMFR with CP-O_3×1 exhibited higher current density compared to CP-Bare and CP-PTFE after the 4-h reaction. Interestingly, the ozone-treated CP demonstrated superior H_2O_2 productivity, as evidenced by the concentration of the produced H_2O_2 (Fig. 6(b)) and H_2O_2 FE (Fig. 6(c)). CP-O_3×1 achieved an FE of 80%, corresponding to 9–13 mM H_2O_2 in the outlet water. The FE of ~80% aligns with results from the CoN$_x$/KB electrocatalyst in RRDE and H-type cell experiments.[12] These findings suggest that the ozone-treated GDL promoted the formation of TPBs at the interface between CoN$_x$/KB, O_2 gas, and water in the zero-gap reactor, which facilitates efficient H_2O_2 removal via water flushing, similar to electrocatalytic reactions in aqueous electrolytes.

In contrast, CP-Bare and CP-PTFE (water contact angles > 130°) showed significantly lower H_2O_2 yield and FE compared to CP-O_3 (contact angle 100°). While PTFE-treated GDLs (with microporous layer) are commonly used in PEFCs to enhance the transport of generated water within the GDE,[32] the high hydrophobicity of CP-PTFE inhibited water flow toward the CoN$_x$/KB electrocatalyst in the PEMFR, resulting in successive reduction of the generated H_2O_2. The moderate wettability of CP-O_3×1 guided water flow to the catalyst, enabling efficient removal of produced H_2O_2. At the Pt/CB anode, the HOR establishes a cell voltage roughly comparable to the potential versus reversible hydrogen electrode (RHE) at low current density. The overvoltage from the current-voltage curve in the PEMFR (Fig. S3(a)) was close to that obtained from the H-type cell experiment in acidic electrolytes.[12]

Ozone-treated GDL arrangement To investigate the effect of ozone treatment on effective H_2O_2 production, the PEMFR was operated using the CP-O_3 GDLs with different ozone-treated sides (flow side, catalyst side, and both sides). Current-time curves showed lower current densities for CP-O_3×1 (catalyst side) and further reduction for CP-O_3×2 (both sides), compared to the CP-O_3×1 (flow side), as shown in Fig. 6(d). Cyclic voltammograms also show a similar trend (Fig. S4(b)). Despite these differences, H_2O_2 FEs remained at approximately 80% for all, and the H_2O_2 concentration corresponding to the current densities was obtained in the outlet water (Figs. 6(e) and (f)). The decreased current densities observed with CP-O_3×1 (catalyst side) likely result from diminished O_2 gas supply caused by water flooding on the catalyst surface. As shown in Figure 2, the untreated side of the CP-O_3×1 retained its hydrophobicity after ozone treatment. When the ozone-treated side faces the flow channel, the slight wettability of the GDL facilitates water flow to collect the produced H_2O_2. In contrast, the hydrophobicity of the back side allows O_2 gas diffusion to the

MEA's catalyst surface. Conversely, placing the ozone-treated GDL on the catalyst side increased water flow on the catalyst surface, but the flooding condition prevented the supply of O_2 gas. Treating both sides of the GDL (CP-O_3×2) and prolonged ozone treatment further hindered the O_2 transport to the catalyst surface due to water flooding.

While the excessive wettability of the GDL reduced the current density, the high hydrophobicity of the GDLs (> 130°) promoted successive H_2O_2 reduction. Therefore, efficient H_2O_2 production in PEMFRs requires a balance between gas diffusivity and wettability in the ozone-treated GDLs to form TPBs and facilitate water flow for efficient product transport. Moderate hydrophobicity on the channel flow side was found to be suitable for this purpose.

The current density gradually declined during 4-h current-time curves (Figs. 6(a) and (d)). Cyclic voltammograms after the 4-h reaction also showed a slight decrease in current density compared to the initial state for all the PEMFRs with CP-O_3 GDLs (Figure S3(c)). However, our previous research has shown that the CoN_x/KB catalyst remains stable during prolonged 2e⁻ ORR.[12] Electrochemical impedance spectroscopy demonstrated no change in the high-frequency resistance of the PEMFR after the reaction, indicating that PEM was not damaged. Therefore, the decline in current density is likely due to the increased GDL wettability induced by ORR.[12]

We have also found that the pretreatment before the electrocatalytic reaction significantly influenced the PEMFR performance (Figure S5). Typically, the cathode was pretreated with water flow (0.50 mL min^{-1}) for 10 min before the reaction at 0.10 V under O_2 (50 mL min^{-1}) and water (0.50 mL min^{-1}). Without pretreatment, the H_2O_2 FE for CP-O_3×1 (catalyst side) was below 20% (Fig. S5(c)). However, pretreatments with water flow for 5 and 10 min increased FE to 35% and 80%, respectively. The highest FE was achieved with a 10-min pretreatment, but the current density was decreased due to water flooding as discussed. These findings highlight the importance of balancing GDL wettability (ozone treatment and water pretreatment) for optimal PEMFR performance.

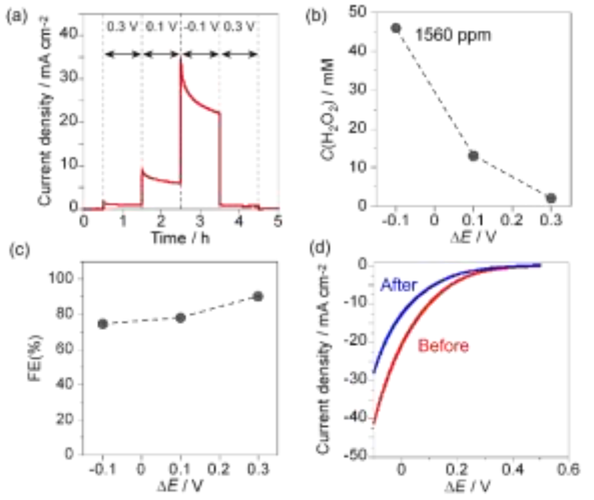

Figure 7. Current-time curve of the PEMFR with CP-O_3 ×1 (flow side) (a), the concentration of produced H_2O_2 (b), and FE of H_2O_2 (c) at different operating voltages; fuel cell mode (0.3 and 0.1 V) and electrolyzer mode (−0.1 V). (d) Cyclic voltammograms before and after the reaction. O_2 and water simultaneously flowed into the cathode at 50- and 0.50-mL min^{-1}, respectively.

Operating cell voltage Figure 7 shows H_2O_2 production with different operating voltages. Current densities for ORR and H_2O_2 concentration were increased with decreasing fuel cell output voltage. The H_2O_2 FE decreased from 90.3% at 0.30 V to 77.8% at 0.10 V owing to the enhanced current density. In electrolysis mode at −0.10 V, current density was significantly enhanced to 20–30 mA cm^{-2}. An H_2O_2 concentration observed in a 1-h continuous reaction was also increased to 46 mM (1560 ppm). The H_2O_2 FE remained at 74.5% even at higher current densities at −0.10 V. The H_2O_2 production rate at −0.10 V reached 345 μmol cm^{-2} h^{-1} (1.38 mmol h^{-1}). To the author's knowledge, the H_2O_2 FE of ~75% was the highest value at 20–30 mA cm^{-2} reported for two-chamber PEM cells for the production of pure H_2O_2 without aqueous electrolyte as an impurity.[21–24] The cyclic voltammogram after the H_2O_2 production showed a slight decrease in the current density compared with the initial state (Fig. 7 (d)). The decay in the current density, which is related to the gradual increase in wettability during ORR, was pronounced at higher current densities.

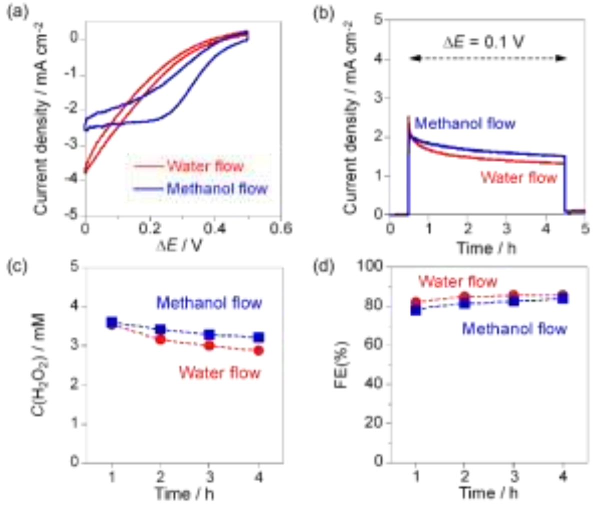

Figure 8. Cyclic voltammograms under the flows of methanol and water (0.50 mL min^{-1}) with O_2 at 50 mL min^{-1}. CP-Bare and CP-O_3×2 GDLs were used for methanol and water, respectively (a). Current-time curves an operating voltage of 0.10 V (b), concentration of produced H_2O_2 (c), and FE of H_2O_2 (d).

Methanol solvent Methanol offers higher O_2 solubility than water, with oxygen mole fractions of 41.5 × 10^{-5} (10 mM) in methanol and 2.30 × 10^{-5} (1.3 mM) in water at 298.15 K and 101 kPa.[33] Direct catalytic synthesis of H_2O_2 in methanol has been reported in several studies.[34–37] In an electrocatalytic system, Huang et al. demonstrated a three-compartment electrolyzer using a hydrogen-permeable Pd foil for H_2O_2 production from O_2 dissolved in methanol-water mixtures.[38] Herein, we investigated the impact of higher dissolved O_2 concentrations in methanol for electrocatalytic H_2O_2 generation, enabling electrolyte-free methanol solutions of H_2O_2 for direct use in organic synthesis.

Figure 8 shows H_2O_2 production in the PEMFR with simultaneous flows of O_2 gas (50 mL min^{-1}) and methanol (0.50 mL min^{-1}) to the cathode. The pristine CP-Bare GDL was selected for the cathode since methanol wets carbon paper more than water. The cyclic voltammogram of methanol flow revealed diffusion-limited current at lower voltages, suggesting that dissolved O_2 in methanol was utilized for the ORR rather than the gaseous O_2 (Fig. 8 (a)). The ORR overpotential in methanol was lower than that in water, but significant hysteresis was observed in the voltammogram. At 0.10 V, a stable current density of 2 mA cm^{-2} and production of ~3.5 mM H_2O_2 (120 ppm) were achieved in methanol flow (Figs. 8 (b) and (c)). Continuous H_2O_2 production was sustained in the PEMFR for 4 h at a rate of 25 µmol cm^{-2} h^{-1} (100 µmol h^{-1}) in methanol. The H_2O_2 FE of ~80% was comparable to that observed in water flow (Fig. 8(d)). These performances, including current density, were similar to those obtained using CP-O_3×2 (both sides treated) in water flow. This similarity is attributed to liquid flooding. However, the cyclic voltammogram (Fig. 8 (a)) indicates that the water system with CP-O_3×2 exhibits Butler-Volmer-like behavior, suggesting that gaseous O_2 is utilized for ORR, unlike in methanol. In contrast, the methanol system displays diffusion-limited current density, despite having ~8-fold higher dissolved O_2 than water, indicating the methanol flooding is severe.

The feasibility of PEMFR for H_2O_2 production must be considered. In PEFCs, H_2O_2 formation as a byproduct accelerates the degradation of perfluorinated sulfonic acid (PFSA) ionomers and membranes (e.g., Nafion), particularly in the presence of metal contaminants like Fe^{2+} and Pt^{2+}, which generate hydroxyl and hydroperoxyl radicals.[39] To mitigate radical-induced PEM degradation, Ce-based radical scavengers are widely used to enhance durability.[40] For methanol-based H_2O_2 production, a key concern is methanol crossover through the PEM. This issue may be addressed by modifying Nafion membranes or developing composite polymer materials to reduce methanol permeability.[41]

Conclusions

The selective production of pure H_2O_2 via electrocatalytic 2e$^-$ ORR was investigated in an H_2–O_2 PEMFR using a CoN_x/KB catalyst. Three GDLs (pristine carbon paper, PTFE-loaded, and ozone-treated) with different hydrophobicity were tested under simultaneous O_2 gas and water flow at the cathode. Supplying only water-dissolved O_2 resulted in low current densities, emphasizing the importance of TPBs formation at the interface of CoN_x/KB electrocatalyst, O_2 gas (50 mL min^{-1}), and water (0.50 mL min^{-1}) for achieving mA cm^{-2}-level ORR. The PEMFR equipped with a CP-O_3×1 GDL on the flow side achieved an H_2O_2 FE of 80%, comparable to previous RRDE and H-type cell experiments under ideal product transportation conditions. In contrast, hydrophobic CP-Bare and CP-PTFE GDLs exhibited low H_2O_2 FE (~15%) due to inhibited water flow, resulting in H_2O_2 retention and successive reduction on the electrocatalyst surface. Enhanced wettability of the flow side of the GDL improved water transport, facilitating efficient H_2O_2 removal. However, ozone treatment on both GDL sides or on the catalyst side decreased current density, suggesting decreased gas diffusivity caused by water flooding. These results highlight that ozone-treated GDLs balance the solvent transport and O_2 diffusion, forming TPBs for 2e$^-$ ORR in the PEMFR. At −0.10 V with current densities of 20–30 mA cm^{-2}, the H_2O_2 production rate was 345 µmol cm^{-2} h^{-1} with 75% FE, producing 1560 ppm H_2O_2 in water without electrolytes. Pure H_2O_2 production in methanol achieved a production rate of 25 µmol cm^{-2} h^{-1} with 80% FE in fuel cell mode without energy input. These findings underscore the importance of optimizing cell design to enhance O_2 gas supply and H_2O_2 transport, maximizing production rates and selectivity in PEM-based zero-gap electrochemical cells.

Author contributions

F.A., T.O., and C.T. wrote the manuscript, and all authors have approved the final version.

Conflicts of interest

There are no conflicts to declare.

Data availability

Research data is available in the main paper and Supplementary Information.

Acknowledgements

This work was supported by the Japan Science and Technology Agency (JST) PRESTO [grant number JPMJPR18T1] and Tokyo Metropolitan University.

References

1 S. Yang, A. Verdaguer-Casadevall, L. Arnarson, L. Silvioli, V. Čolić, R. Frydendal, J. Rossmeisl, I. Chorkendorff and I. E. L. Stephens, *ACS Catal.*, 2018, **8**, 4064–4081.
2 Q. Zhi, R. Jiang, X. Yang, Y. Jin, D. Qi, K. Wang, Y. Liu and J. Jiang, *Nat. Commun.*, 2024, **15**, 678.
3 X. Zhang, H. Su, P. Cui, Y. Cao, Z. Teng, Q. Zhang, Y. Wang, Y. Feng, R. Feng, J. Hou, X. Zhou, P. Ma, H. Hu, K. Wang, C. Wang, L. Gan, Y. Zhao, Q. Liu, T. Zhang and K. Zheng, *Nat. Commun.*, 2023, **14**, 7115.
4 Y. Tian, D. Deng, L. Xu, M. Li, H. Chen, Z. Wu and S. Zhang, *Nano-Micro Lett.*, 2023, **15**, 122.
5 Y. Yi, L. Wang, G. Li and H. Guo, *Catal. Sci. Technol.*, 2016, **6**, 1593–1610.
6 Q. Zhang, X. Tan, N. M. Bedford, Z. Han, L. Thomsen, S. Smith, R. Amal and X. Lu, *Nat. Commun.*, 2020, **11**, 4181.
7 K. Otsuka and I. Yamanaka, *Electrochim. Acta*, 1990, **35**, 319–322.
8 C. Xia, Y. Xia, P. Zhu, L. Fan and H. Wang, *Science*, 2019, **366**, 226–231.

9 Y. Xia, X. Zhao, C. Xia, Z.-Y. Wu, P. Zhu, J. Y. Kim, X. Bai, G. Gao, Y. Hu, J. Zhong, Y. Liu and H. Wang, *Nat. Commun.*, 2021, **12**, 4225.

10 Y. Pang, H. Xie, Y. Sun, M.-M. Titirici and G.-L. Chai, *J. Mater. Chem. A*, 2020, **8**, 24996–25016.

11 H. W. Kim, V. J. Bukas, H. Park, S. Park, K. M. Diederichsen, J. Lim, Y. H. Cho, J. Kim, W. Kim, T. H. Han, J. Voss, A. C. Luntz and B. D. McCloskey, *ACS Catal.*, 2020, **10**, 852–863.

12 T. Okazaki, K. Shibata, C. Tateishi, K. Enomoto, K. Beppu and F. Amano, *ACS Sustain. Chem. Eng.*, 2024, **12**, 9856–9863.

13 V. Mehta and J. S. Cooper, *J. Power Sources*, 2003, **114**, 32–53.

14 J. Ge, A. Higier and H. Liu, *J. Power Sources*, 2006, **159**, 922–927.

15 J. Wang, C. Li, M. Rauf, H. Luo, X. Sun and Y. Jiang, *Sci. Total Environ.*, 2021, **759**, 143459.

16 E. Jung, H. Shin, W. Hooch Antink, Y.-E. Sung and T. Hyeon, *ACS Energy Lett.*, 2020, **5**, 1881–1892.

17 J. An, N. Li, Q. Zhao, Y. Qiao, S. Wang, C. Liao, L. Zhou, T. Li, X. Wang and Y. Feng, *Water Res.*, 2019, **164**, 114933.

18 S. A. Hejazi and F. Taghipour, *Electrochim. Acta*, 2023, **439**, 141695.

19 Z. Chen, S. Chen, S. Siahrostami, P. Chakthranont, C. Hahn, D. Nordlund, S. Dimosthenis, J. K. Nørskov, Z. Bao and T. F. Jaramillo, *React. Chem. Eng.*, 2017, **2**, 239–245.

20 I. Yamanaka, R. Ichihashi, T. Iwasaki, N. Nishimura, T. Murayama, W. Ueda and S. Takenaka, *Electrochim. Acta*, 2013, **108**, 321–329.

21 T. Iwasaki, Y. Masuda, H. Ogihara and I. Yamanaka, *Electrocatalysis*, 2018, **9**, 236–242.

22 W. Li, A. Bonakdarpour, E. Gyenge and D. P. Wilkinson, *ChemSusChem*, 2013, **6**, 2137–2143.

23 W. Li, A. Bonakdarpour, E. Gyenge and D. P. Wilkinson, *J. Appl. Electrochem.*, 2018, **48**, 985–993.

24 H. Li, P. Wen, D. S. Itanze, Z. D. Hood, S. Adhikari, C. Lu, X. Ma, C. Dun, L. Jiang, D. L. Carroll, Y. Qiu and S. M. Geyer, *Nat. Commun.*, 2020, **11**, 1–12.

25 J. C. Jiménez-García, D. F. F. Robledo Flores, R. H. Acosta, M. I. Velasco, E. A. Franceschini and M. M. Mariscal, *Int. J. Hydrogen Energy*, 2024, **52**, 65–71.

26 T. L. Doan, H. E. Lee, S. S. H. Shah, M. J. Kim, C. H. Kim, H. S. Cho and T. Kim, *Int. J. Energy Res.*, 2021, **45**, 14207–14220.

27 X. R. Wang, Y. Ma, J. Gao, T. Li, G. Z. Jiang and Z. Y. Sun, *Int. J. Hydrogen Energy*, 2021, **46**, 12206–12229.

28 F. B. Baz, R. M. Elzohary, S. Osman, S. A. Marzouk and M. Ahmed, *Energy Convers. Manag.*, 2024, **302**, 118150.

29 H. Kim, Y.-J. Lee, D. Lee, G. Park and Y. Yoo, *Carbon N. Y.*, 2013, **60**, 429–436.

30 H.-L. Chiang, P. . Chiang and C. . Huang, *Chemosphere*, 2002, **47**, 267–275.

31 E. M. Miner, T. Fukushima, D. Sheberla, L. Sun, Y. Surendranath and M. Dincă, *Nat. Commun.*, 2016, **7**, 10942.

32 M. Mortazavi and K. Tajiri, *J. Power Sources*, 2014, **245**, 236–244.

33 H. Miyamoto, Y. Yampolski and C. L. Young, *J. Phys. Chem. Ref. Data*, 2014, **43**, 033102.

34 T. Moreno, J. García-Serna and M. J. Cocero, *Green Chem.*, 2010, **12**, 282–289.

35 F. MENEGAZZO, P. BURTI, M. SIGNORETTO, M. MANZOLI, S. VANKOVA, F. BOCCUZZI, F. PINNA and G. STRUKUL, *J. Catal.*, 2008, **257**, 369–381.

36 T. Moreno, J. García-Serna, P. Plucinski, M. J. Sánchez-Montero and M. J. Cocero, *Appl. Catal. A Gen.*, 2010, **386**, 28–33.

37 Z. Yang, Z. Wei, S. Zhou, B. Bao, S. Zhao and F. Gong, *Chem. Eng. J.*, 2023, **456**, 140915.

38 A. Huang, R. S. Delima, Y. Kim, E. W. Lees, F. G. L. Parlane, D. J. Dvorak, M. B. Rooney, R. P. Jansonius, A. G. Fink, Z. Zhang and C. P. Berlinguette, *J. Am. Chem. Soc.*, 2022, **144**, 14548–14554.

39 K. Hongsirikarn, X. Mo, J. G. Goodwin and S. Creager, *J. Power Sources*, 2011, **196**, 3060–3072.

40 G. Li, W. Zheng, X. Li, S. Luo, D. Xing, P. Ming, B. Li and C. Zhang, *Int. J. Hydrogen Energy*, 2024, **74**, 17–30.

41 M. Ahmed and I. Dincer, *Int. J. Energy Res.*, 2011, **35**, 1213–1228.

Data availability

Research data is available in the main paper and Supplementary Information.